

First ENA observations at Mars: Solar-wind ENAs on the nightside

K. Brinkfeldt^{a,*}, H. Gunell^{a,b}, P. C:son Brandt^c, S. Barabash^a, R.A. Frahm^d, J.D. Winningham^d,
E. Kallio^e, M. Holmström^a, Y. Futaana^a, A. Ekenbäck^a, R. Lundin^a, H. Andersson^a,
M. Yamauchi^a, A. Grigoriev^a, J.R. Sharber^d, J.R. Scherrer^d, A.J. Coates^f, D.R. Linder^f,
D.O. Kataria^f, H. Koskinen^e, T. Säles^e, P. Riihelä^e, W. Schmidt^e, J. Kozyra^g, J. Luhmann^h,
E. Roelof^c, D. Williams^c, S. Livi^c, C.C. Curtisⁱ, K.C. Hsiehⁱ, B.R. Sandelⁱ, M. Grande^j, M. Carter^j,
J.-A. Sauvaud^k, A. Fedorov^k, J.-J. Thocaven^k, S. McKenna-Lawler^b, S. Orsini^l, R. Cerulli-Irelli^l,
M. Maggi^l, P. Wurz^m, P. Bochsler^m, N. Kruppⁿ, J. Wochⁿ, M. Fränzⁿ, K. Asamura^o, C. Dierker^p

^a Swedish Institute of Space Physics, Box 812, S-98 128 Kiruna, Sweden

^b Space Technology Ltd., National University of Ireland, Maynooth, Co. Kildare, Ireland

^c Applied Physics Laboratory, Johns Hopkins University, Laurel, MD 20723-6099, USA

^d Southwest Research Institute, San Antonio, TX 7228-0510, USA

^e Finnish Meteorological Institute, Box 503, FIN-00101 Helsinki, Finland

^f Mullard Space Science Laboratory, University College London, Surrey RH5 6NT, UK

^g Space Physics Research Laboratory, University of Michigan, Ann Arbor, MI 48109-2143, USA

^h Space Science Laboratory, University of California in Berkeley, Berkeley, CA 94720-7450, USA

ⁱ University of Arizona, Tucson, AZ 85721, USA

^j Rutherford Appleton Laboratory, Chilton, Didcot, Oxfordshire OX11 0QX, UK

^k Centre d'Etude Spatiale des Rayonnements, BP-4346, F-31028 Toulouse, France

^l Istituto di Fisica dello Spazio Interplanetari, I-00133 Rome, Italy

^m Physikalisches Institut, University of Bern, CH-3012 Bern, Switzerland

ⁿ Max-Planck-Institut für Aeronomie, D-37191 Katlenburg-Lindau, Germany

^o Institute of Space and Astronautical Science, 3-1-1 Yoshinodai, Sagamichara, Japan

^p Technical University of Braunschweig, Hans-Sommer-Strasse 66, D-38106 Braunschweig, Germany

Received 11 April 2005; revised 27 August 2005

Available online 13 February 2006

Abstract

We present measurements with an Energetic Neutral Atom (ENA) imager on board Mars Express when the spacecraft moves into Mars eclipse. Solar wind ions charge exchange with the extended Mars exosphere to produce ENAs that can spread into the eclipse of Mars due to the ions' thermal spread. Our measurements show a lingering signal from the Sun direction for several minutes as the spacecraft moves into the eclipse. However, our ENA imager is also sensitive to UV photons and we compare the measurements to ENA simulations and a simplified model of UV scattering in the exosphere. Simulations and further comparisons with an electron spectrometer sensitive to photoelectrons generated when UV photons interact with the spacecraft suggest that what we are seeing in Mars' eclipse are ENAs from upstream of the bow shock produced in charge exchange with solar wind ions with a non-zero temperature. The measurements are a precursor to a new technique called ENA sounding to measure solar wind and planetary exosphere properties in the future.

© 2006 Elsevier Inc. All rights reserved.

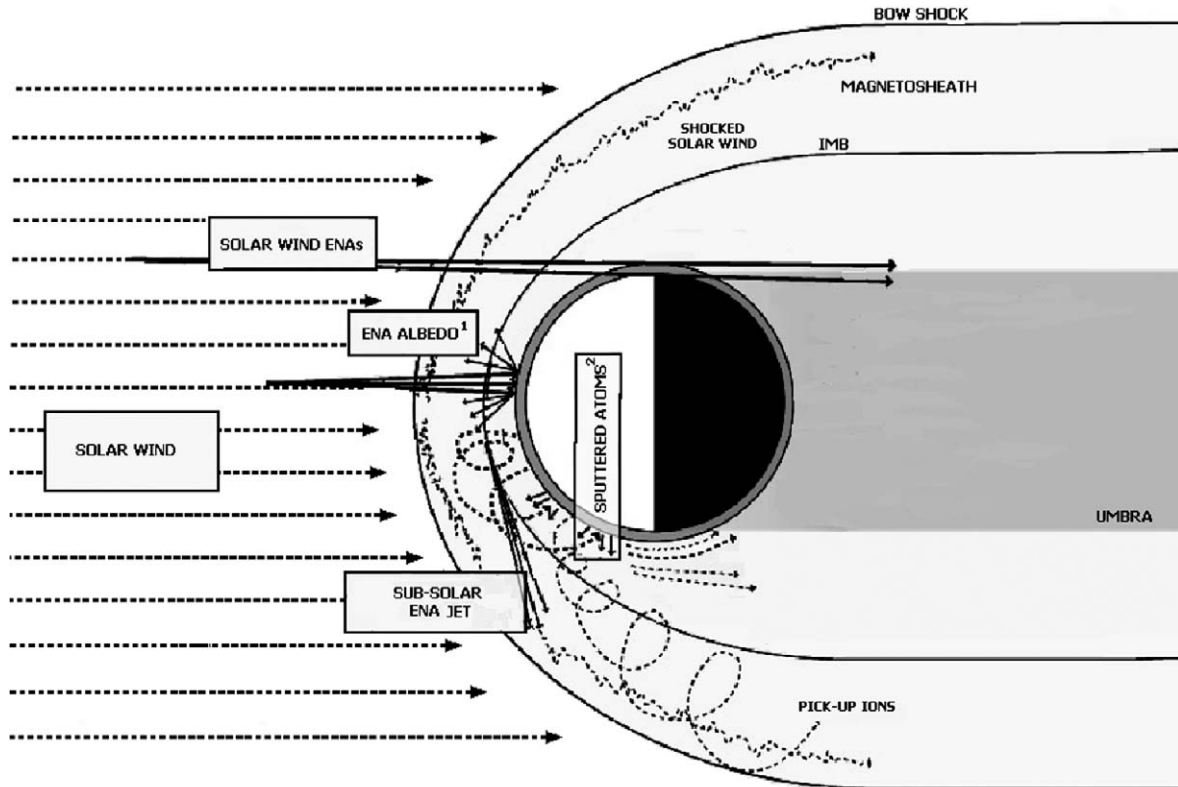
Keywords: Mars; Solar wind; Magnetospheres

1. Introduction

Energetic Neutral Atom (ENA) imaging remotely images the interaction between singly charged ions (or molecules) and

* Corresponding author.

E-mail address: klas@irf.se (K. Brinkfeldt).



¹ Sputtering from solar wind ENAs [Kallio et al., 1997]
² Sputtering from re-impacting pick-up ions [Luhmann and Kozyra, 1991]

Fig. 1. Illustration of the ENA production regions at Mars from models. Solar wind ENAs are produced by charge exchange between the solar wind ions and the extended exosphere in front of the bow shock. The ENA albedo are produced by the solar wind ENAs and pick-up ions precipitating the upper atmosphere (Futaana et al., 2006a). The subsolar ENA jet is produced where the subsolar deflection point of the solar wind flowlines occurs in high neutral gas density close to the planet (Futaana et al., 2006b; Gunell et al., 2005).

neutral gas and can be used to diagnose both. At Earth several missions (Barabash et al., 1998; Mitchell et al., 2000, 2003; McKenna-Lawlor et al., 2005) have used ENA imaging to image the ring current and plasma sheet (Brandt et al., 2001, 2002). Collier et al. (2001) report on measured solar wind ENAs from within the Earth's magnetosphere. It is estimated that the neutral flux is $\approx 10^{-3}$ – 10^{-4} of the solar wind flux. A recent study (Taguchi et al., 2004) has shown that such observations can be used to monitor the cusp motion, which responds to large variations of IMF Bz.

For the first time, ENA imaging at Mars is carried out by the Neutral Particle Imager (NPI) on the Analyzer of Space Plasmas and Energetic Atoms (ASPERA-3) experiment (Barabash et al., 2004) on board the Mars Express mission. Detecting ENAs in the low-energy range has proven a challenging technique to master. Up to now three missions have carried or carry ENA instruments in the sub-keV range: the PIPPI (Prelude In Planetary Particle Imaging) imager on board the Astrid-1 mission (Barabash et al., 1998; Brandt et al., 2001), the LENA (Low Energy Neutral Particle) imager on board the IMAGE mission (Moore et al., 2000), and the NPI and the NPD (Neutral Particle Detector) on board Mars Express.

The solar wind interaction with Mars is complex and produces ENAs in a wide energy range whose detection allows the

interaction to be studied. Fig. 1 is a sketch of the expected ENA emissions around Mars. Three main ENA production areas have been identified in simulations (Kallio et al., 1997): (1) in the solar wind upstream of the bow shock (BS), (2) downstream of the BS in the magnetosheath, (3) downstream of the induced magnetosphere boundary (IMB, as defined by Lundin et al., 2004) near the planetary obstacle. Simulations of the ENA production in the solar wind and the magnetosheath region have been presented by Holmström et al. (2002). In this paper we report NPI observations showing how significant flux of ENAs produced upstream of the bow shock penetrates the martian system.

In the next section we describe the NPI sensor and observations as the spacecraft enters the eclipse. In Section 3 we discuss the origin of the detected ENA signal and the contribution from scattered UV photons. We also treat the observed variations between different orbits and introduce ENA sounding as a new measurement technique.

2. Observations

The NPI is a part of the ASPERA-3 instrument on board Mars Express (Barabash et al., 2004) and measures ENA in the energy range 100 eV–60 keV, where the highest energy is the deflector cut-off for the maximum applied voltage. ASPERA-3 also includes two identical neutral particle detectors (NPD 1

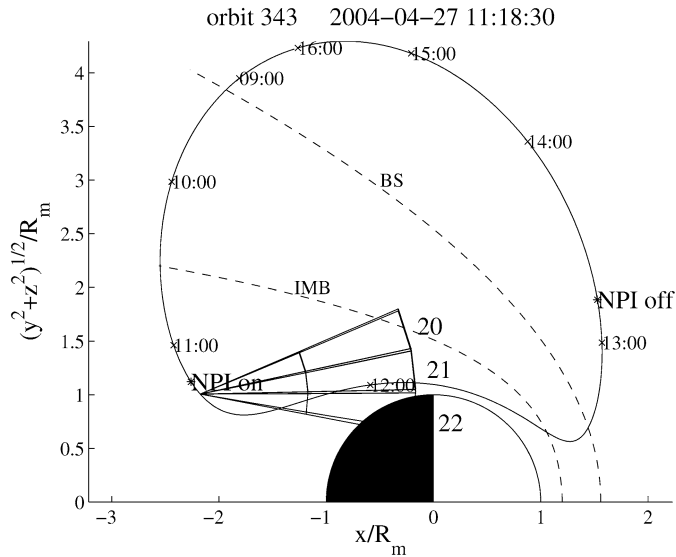


Fig. 2. A view of the orbit geometry with the field of view of NPI sectors 20–22 at 11:18:30 UT during orbit 343 on April 27, 2004. The plot is in cylindrical coordinates (see text). UT hours are included in the plot. Distances are in Mars' radii ($R_m = 3397$ km). The area between the bow shock (BS) and the induced magnetosphere boundary (IMB) is referred to as the magnetosheath.

and 2), an electron spectrometer (ELS) and an ion mass analyzer (IMA). NPD has energy and mass resolution but poor angular resolution, while the NPI is a pure imager without energy or mass resolution, but higher angular resolution. NPD measurements from Mars' dayside are reported by Futaana et al. (2006a, 2006b).

The NPI is a 360° ENA imager sectioned into 32 sectors, each with a $11.25^\circ \times 4.0^\circ$ field of view. Charged particles are rejected in an electrostatic deflection system. The neutrals hit a central target block and are reflected towards a microchannel plate (MCP). The MCP overlays a 32 sector anode from which we derive directional information. UV rejection is based on blackening of the deflection system and target block surfaces. The UV photon detection efficiency for Lyman alpha (L_α) photons ($\lambda = 121.6$ nm), as established from UV calibrations on the NPI reference model, is 10^{-5} . The NPI aperture plane coincides with the ecliptic plane in most considered orbits. This results in a very high count rate from direct solar photons ($>10^5$ s $^{-1}$) in the NPI. This affects all sectors, not just the ones pointing towards the Sun, rendering ENA measurements from any direction impossible. The observations here are obtained in the sunward direction. In order to minimize UV contamination we focus on NPI measurements during the spacecraft's transition into Mars eclipse. A typical view of the orbit geometry with the field of view of NPI sectors 20–22 is shown in Fig. 2. The plot is a cylindrical representation of a Mars centered right-handed coordinate system, in which the x -axis points towards the Sun and the z -axis points northward perpendicular to the ecliptic plane. In the plot $(y^2 + z^2)^{1/2}$ is thus the distance to the Mars–Sun line.

The measured count rates for sectors 17–28 during the entry into eclipse on orbit 343, April 27, 2004 are shown in Fig. 3a. Figs. 3b and 3c show count rates from an ENA simulation (see

Section 3.1). Fig. 4 shows the measurement at 11:22 UT in a fish-eye view (see Holmström et al., 2002), that may provide a better understanding of the NPI field of view.

As the spacecraft moves deeper into eclipse there is a lasting response in the sectors pointing in the direction of the Sun. First there is a sharp drop in the count rate (see Fig. 3a). This is common in all eclipse transitions and can be explained by the direct solar photon flux disappearing when the Sun sets below Mars' limb. When the count rate has dropped to around 10^2 s $^{-1}$ there is an abrupt change in the slope and the count rate exhibits an exponential decrease that lasts for typically 5–8 min. The count rate then reaches the background level of the NPI at around 10 s $^{-1}$ /sector. This long lasting signal is the subject of this analysis.

Fig. 5 shows some typical NPI count rates as the spacecraft enters eclipse between April 23, 2004 and May 14, 2004. The count rate is plotted against the parameter h , which is defined in Fig. 6. For clarity the signals are smoothed using

$$S_i = \begin{cases} \frac{1}{w} \sum_{j=0}^{w-1} C_{i+j-w/2}, & i = (w+1)/2, \dots, N-w, \\ C_i, & \text{otherwise,} \end{cases}$$

where S_i is the new, smooth, data point, w is the width of the smoothing box, C_i is the original data point, and N is the total number of data points. A width of $w = 59$ s was used here. The signal demonstrates a clear variability. Some orbits show a response lasting longer and there can be a flat region in the count rate after the initial decrease (for example, orbits 343 and 362 in Fig. 5). Other orbits exhibit a more direct decrease in count rate (for example, orbits 344 and 363 in Fig. 5).

3. Discussion

3.1. Comparison with simulations

The ENA simulations we have used are based on an empirical model of the solar wind protons and recent models of the Mars exosphere as described by Kallio (1996) and Holmström et al. (2002). The model calculates line of sight integrals from ENA source regions to the detector with the assumption that the environment is optically thin for ENAs outside an impenetrable obstacle with a radius of 1.05 Mars radii. In the simulation we have placed a virtual NPI in the correct orbit position. To calculate the NPI count rate, the calibrated angular response function, the relative directional sensitivities, and efficiencies have been used. The parameters used in the simulations are given in Table 1. See also Gunell et al. (2005) for a more detailed description and Gunell et al. (2006) for a comparison of different simulation models.

With the NPI sensitivity to UV photons in mind it is not trivial to determine whether the lingering signals are caused by ENA or scattered UV. The difficulties lie in the fact that ENA and UV are scattered from the same region and should exhibit roughly the same exponential decrease with altitude above the martian limb. We have made a simplified simulation of ultraviolet light from Lyman alpha airglow to investigate the possible contamination of the data by UV photons. The model is based

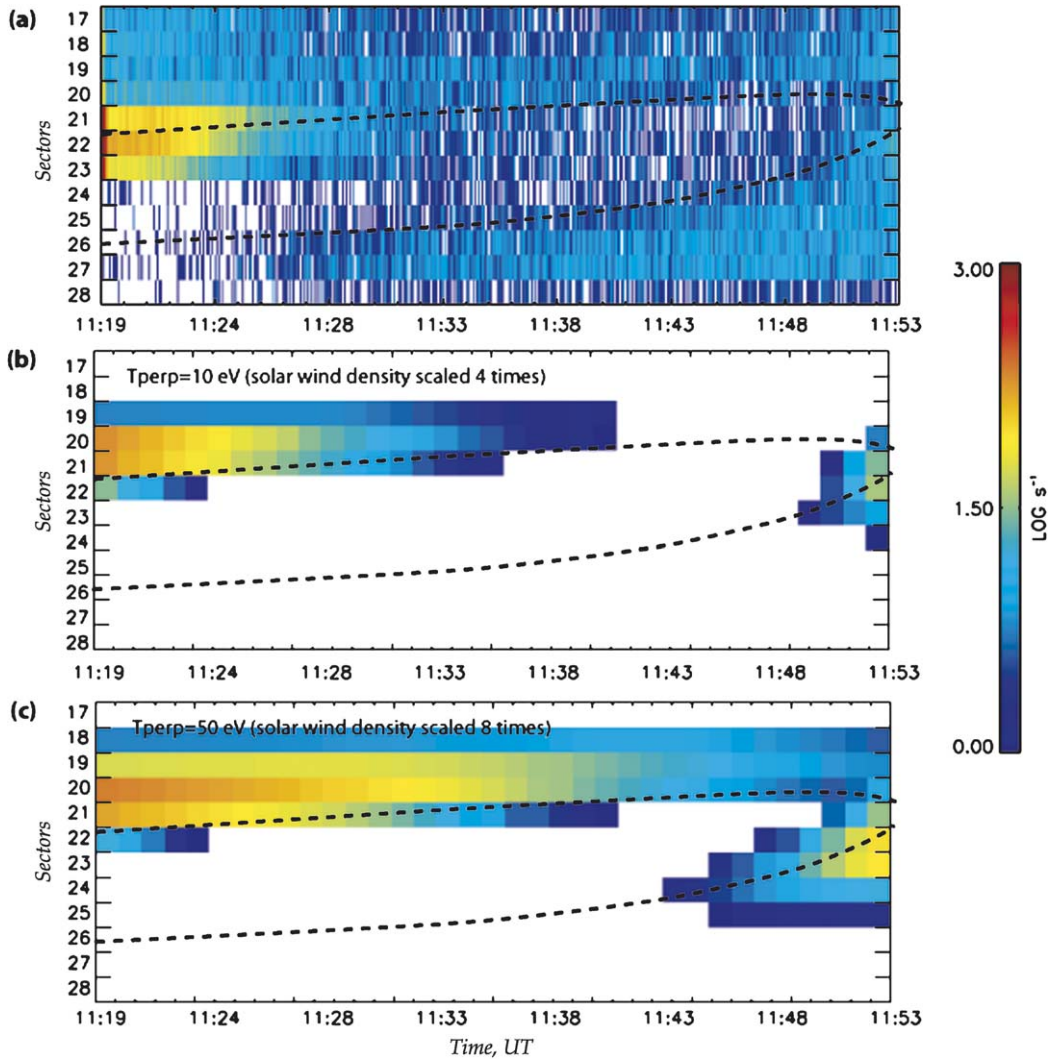


Fig. 3. (a) NPI measurements obtained in eclipse on April 27, 2004 (orbit 343). A distinct signal was observed in sectors 20–23 lasting deep into the umbra. The y-axis is sector number (direction) and x-axis is time in UT. The color scale indicates count rate (s^{-1}). The dashed lines are the plotted martian limbs as viewed from the NPI. (b) Simulations using a semiempirical solar wind flow model with a temperature of 10 eV. (c) Simulations using a semiempirical solar wind flow model with a temperature of 50 eV. The ENAs are produced via charge exchange of the upstream solar wind with the extended martian exosphere and can propagate into the umbra due to the temperature spread and appear in sectors 19–22. The additional counts observed in sector 23 may be an effect of a sector priority, in which sectors with higher numbers are prioritized for simultaneous pulses.

on Bush and Chakrabarti (1995a), but is simplified by assuming only single scattering of the incident sunlight. The count rate R_{UV} caused by UV photons is estimated by a line of sight integral

$$R_{UV} = A\sigma Q \frac{\Omega}{4\pi} \int_{LOS} S_{\text{sun}} e^{-\tau(s)} ds, \quad (1)$$

where τ is the optical depth along the line of sight:

$$\tau(s) = \sigma \int_0^s n_{\text{H}}(s') ds' \quad (2)$$

and $A = 5.25 \times 10^{-5} \text{ m}^2$ is the detector area, $\sigma = 1.19 \times 10^{-17} \cdot \sqrt{T_0/T_{\text{H}}} \text{ m}^2$ is the photo absorption cross section (Bush and Chakrabarti, 1995b), where $T_0 = 1000 \text{ K}$. $Q = 5 \times 10^{-6}$ is the photon detection efficiency of the NPI, Ω the solid angle of the

field of view, and n_{H} is the density of neutral hydrogen in the exosphere. The source function S_{sun} is given by

$$S_{\text{sun}}(x, y, z) = \phi_s \int_x^{x_0} e^{-\tau(x', y, z)} dx', \quad (3)$$

where $x_0 = 20 R_{\text{m}}$ is the sunward edge of the simulation region, $\phi = 2.81 \times 10^{13} \text{ m}^{-2} \text{ s}^{-1}$ is the incident Lyman alpha flux within the Doppler bandwidth. The value for the solar Lyman alpha is obtained from the Solar2000 model (Tobiska et al., 2000) and is scaled by the square ratio of the Earth–Sun and Mars–Sun distances and the Doppler bandwidth to solar emission line bandwidth ratio (Bush and Chakrabarti, 1995a). Finally τ is defined by

$$\tau = \sigma \int_x^{x_0} n_{\text{H}}(x') dx', \quad (4)$$

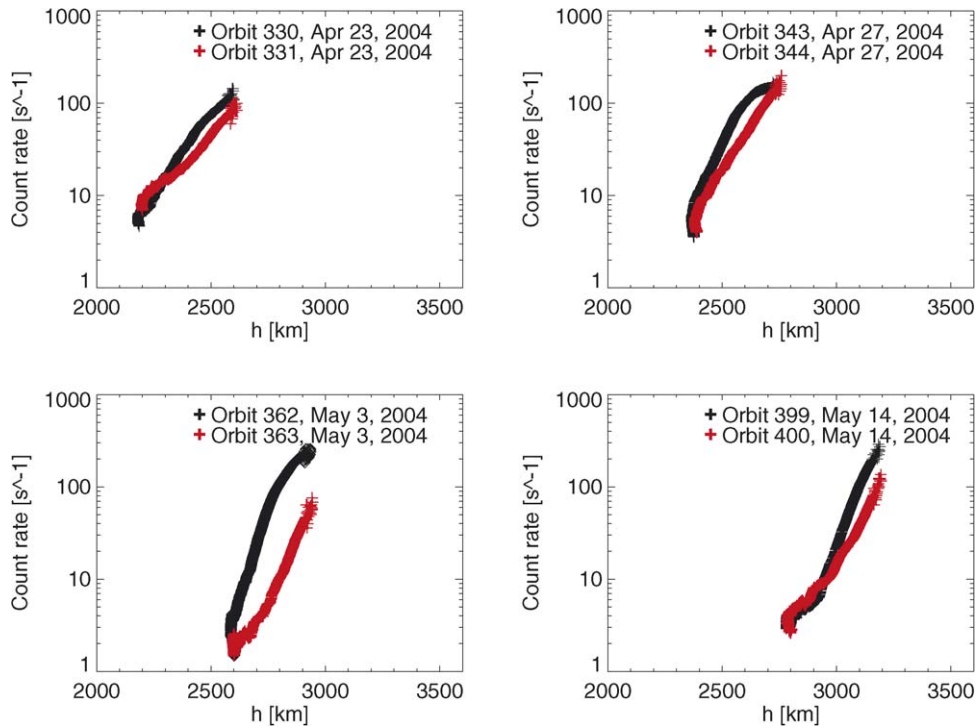


Fig. 5. Count rate data from NPI sector 22 during selected orbits between April 27, 2004 and May 14, 2004. The parameter h is the shortest distance from the center of Mars to the vector from the center of sector 22 (see Fig. 4).

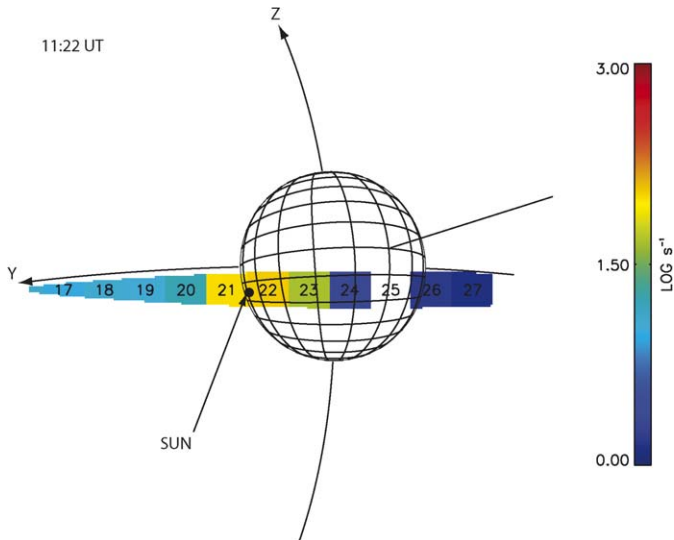


Fig. 4. A fish-eye view of the observed ENA emissions at around 11:22 UT. The image resembles what a human eye would see. Ecliptic north is along the z -axis and the x -axis points towards the Sun. The dot represents the location of the Sun and is hidden behind the planet. The color scale indicates count rate (s^{-1}).

where the path of integration is parallel with the x -axis and runs from the source point in question to $x = x_0$. As with the ENA simulation the calibrated response function is used. The flight model NPI on board Mars Express was not calibrated against UV. The photon detection efficiency, and the relative directional sensitivities are from calibrations of an NPI reference model. This introduces an uncertainty in the absolute count rate, but the simulation result can still serve as a relative measure of the

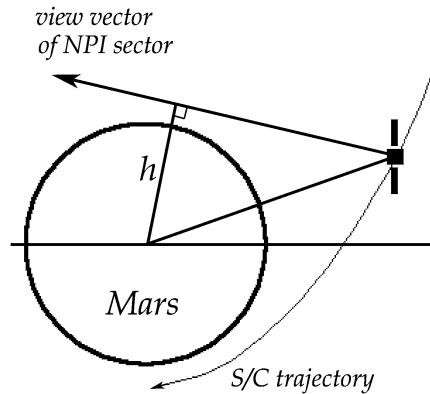


Fig. 6. A parameter h is defined as the shortest distance to the NPI center sector view vector from the center of the planet.

contribution from UV light, and the shape of the scaled curves shown can be compared to the shape of the count rates in Fig. 7. Our simple UV model does not take into account direct photons from the Sun, and mechanisms other than L_α airglow that can scatter UV photons into the umbra are not included.

Fig. 7 is a plot of the ENA and UV simulations overlaid on the count rate from sectors 20, 21, and 22. The photon related count rate is negligible in all other sectors during this time interval. Sectors 20 and 21 follow the ENA simulation reasonably well, while sector 22 has too high count rate. This could partly be due to ENA scattering in the exosphere (Kallio et al., 2006), but also to a priority effect in the sensor, in which sectors with higher numbers are prioritized for simultaneous pulses. The effect was found during calibrations of the NPI and is explained as an increase of the noise in the neighboring sectors

when there is a hit in one sector. When a hit on one of the sectors is registered the NPI logic starts at the highest numbered

Table 1
Model parameters used in this work

Parameters	
Solar wind	
Plasma density	$2.5 \times 10^6 \text{ m}^{-3}$
Temperature	10, 20, 30, and 50 eV
Solar wind speed	400 km/s
Geometry	
Bow shock position	$1.55 R_m$
IMB position	$1.2 R_m$
IMB penetration	1/6
Neutral exobase	
H density	$9.9 \times 10^{11} \text{ m}^{-3}$
H temperature	192 K
H ₂ density	$3.8 \times 10^{12} \text{ m}^{-3}$
H ₂ temperature	192 K
He density	$7.2 \times 10^{11} \text{ m}^{-3}$
He temperature	275 K
O _{hot} density	$5.5 \times 10^9 \text{ m}^{-3}$
O _{hot} temperature	$4.4 \times 10^3 \text{ K}$
O _{thermal} density	$1.4 \times 10^{14} \text{ m}^{-3}$
O _{thermal} temperature	173 K

Model parameters are identical to the parameters used by Holmström et al. (2002) except we have run it with different solar wind temperatures (Holmström et al. (2002) used 10 eV). The exobase is located at 170 km altitude.

sector (sector 31) and checks it for the hit. If sector 31 has not registered the count it checks sector 30, 29, 28 and so on until it encounters the sector with the count. However, simultaneous noise in the neighbor with a higher sector number often cause the logic to register a hit in that sector instead. There is then a build-in priority effect toward higher numbered sectors for any counts that occur simultaneously (within ≈ 200 ns). From calibrations the effect could be responsible for up to 50% of the count rate that end up in the higher sector. Efforts to study this effect further and compensate for it are ongoing.

Not only is the expected UV photon count rate orders of magnitude too low to explain the signal, the curve shape is different. The slope of the UV count rate is consistently higher than the slope of the data count rate for all three sectors. Note that the direct solar photons are not modeled, which is why we do not see a high UV count rate when we are outside of the eclipse in the beginning of the figure.

3.2. NPI signal vs photoelectron flux

To further investigate if the signal is due to UV photons or not we compare the NPI observations with photoelectron measurements from the electron spectrometer ELS. Since the flux of photoelectrons emitted by the spacecraft is proportional to the incident UV photon flux, the ELS measurements can serve as an indicator of the photon flux variations. We thus examine

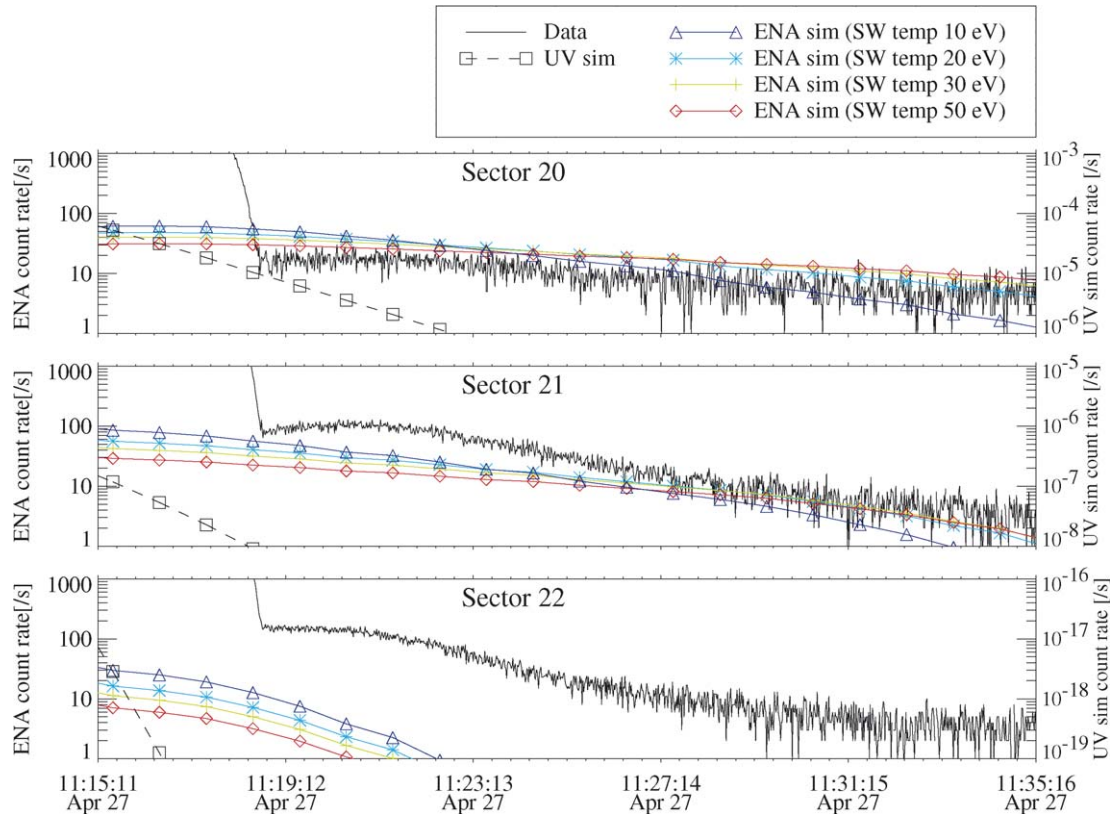


Fig. 7. NPI count rates from sectors 20, 21, and 22 (solid line) during the transition into eclipse on orbit 343 (April 27, 2004). ENA simulations with a virtual NPI sensor are overlotted. ENA simulations count rate and the observed data count rate in each plot are on the left y-axis. The simulations do not include scattering of ENAs in Mars' exosphere. The dashed line with squares is a UV simulation with a virtual NPI sensor. The simulated UV count rate in each plot is on the right y-axis. The extremely low count rate of UV suggests that the observations are ENAs.

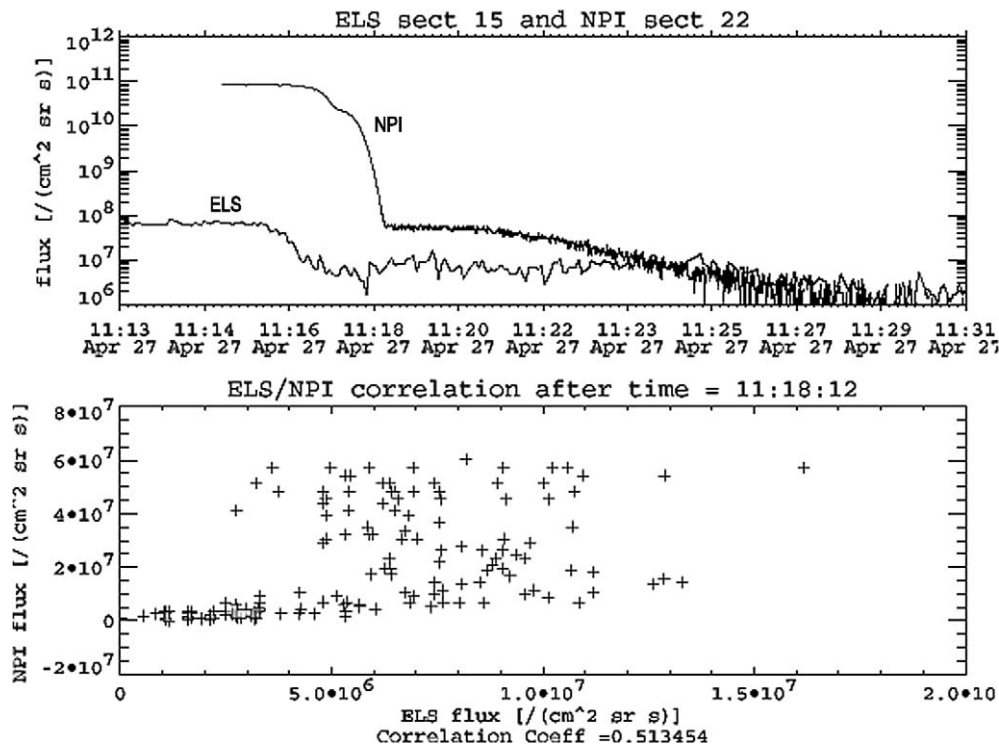


Fig. 8. The top panel is a comparison of the particle fluxes measured by NPI and ELS, when entering eclipse. The ELS flux is integrated between 5 and 10 eV, and is a measure of photoelectron production on the spacecraft surfaces. It can thus give an indication of the UV background. The lower panel shows the dependence of the normalized NPI flux on the normalized ELS flux. No correlation is observed.

the correlation between the NPI signal and ELS photoelectron measurements. An ELS sector viewing across the spacecraft has the best potentiality to observe photoelectrons emitted from the spacecraft.

ELS sector 15 was selected, which has full viewing across the spacecraft and should detect the highest rate of spacecraft photoelectrons. The ELS electron energy spectrum from sector 15 is integrated from 5 eV (the internal protection grid potential) to 10 eV (estimated spacecraft potential) to determine the integral electron flux that is locally produced.

The ELS integral electron flux is compared to the NPI integral ENA flux in Fig. 8 for orbit 343 on April 27, 2004 (see Appendix A for count rate to flux conversion). The typical scenario is that as the Sun vanishes behind the planet, first ELS observes a decrease in atmospherically generated photoelectrons of about an order of magnitude as they wind their way to the spacecraft (thus a remote measurement of sunset in the atmosphere). Shortly after the ELS decrease, the NPI photon flux starts dropping from 10^{11} as the NPI also observes the Sun set in the martian atmosphere. The lower panel of Fig. 8 shows the dependence of the NPI normalized flux on the ELS normalized flux after the initial drop in NPI count rate (i.e., after 11:18:12 UT). There exist some correlations for low flux when the count rate in the NPI decrease close to noise level, but none for higher NPI fluxes.

3.3. Signal variability and ENA sounding

Fig. 5 shows a selection of NPI signals during eclipse transitions between April 23, 2004 and May 14, 2004. There is a clear

variability between consecutive orbits, which is on a short time scale (orbit period is ≈ 7.5 h). One can rule out that this variation is due only to changes in the orbit geometry (because the orbit geometry and spacecraft attitude changes only marginally between consecutive orbits). Therefore it must be an effect of changing physical conditions around the planet.

For example, changes in the local exosphere density could give this effect. A denser exosphere causes more collisions in which an ENA can change direction and end up in eclipse. Kallio et al. (2006) present Monte Carlo simulations of such scattering and find that the ENA flux due to this mechanism is very low in eclipse. Variations in exosphere density are thus not likely to cause the variation in the NPI signal.

A more likely candidate is a change in the solar wind ion temperature. A change in the solar wind temperature would cause the produced ENAs to scatter at wider angles from the solar wind direction, allowing them to reach further into eclipse. The scattering angle should be on the order of $\alpha \approx \arctan \sqrt{kT_{\text{sw}}/E_{\text{sw}}}$, where T_{sw} is solar wind temperature, E_{sw} is solar wind energy, and k is Boltzmann's constant. The ENA simulations with different solar wind temperature are shown in Fig. 7. According to the simulations a signal that is lower in intensity as the NPI enters eclipse, but lasts longer into the eclipse is expected for higher solar wind temperatures. Both are expected effects of increased ENA spreading from the solar wind direction with temperature.

As a third possibility for the cause of the variation between orbits we would like to mention the recently discovered crustal magnetic fields on Mars (Acuña et al., 1998). Solar wind temperature cannot account for all the variability in the

observations. Some orbits (as orbit 343 in Fig. 7) have a pronounced flat region before the exponential decrease that extends beyond the simulated signals. It has been suggested that the crustal magnetic field can facilitate ion and electron accelerations and are sites of large outflows (and inflows) of particles (Acuña et al., 1999; Mitchell et al., 2001; Lundin et al., 2004, 2006). If such an outflow of ions were to coincide with the position of the spacecraft as it enters eclipse on one orbit but not the next, ENAs resulting from charge exchange with such ions may be what causes the measured variations. Further investigations of the reason for these variations are ongoing.

The NPI observations constitute a precursor measurement to the new ENA sounding technique also presented in Kallio et al. (2006). From ENA measurements in the eclipse one may be able to extract physical properties of the solar wind and exosphere. Similar to radio occultation measurements, the spreading angle, i.e., how far into eclipse one can measure scattered ENAs, is one measurement that can facilitate a deeper understanding of the exosphere properties. Energy dispersion is another. To take full advantage of this technique, however, requires also energy resolution, which is not provided by the NPI.

4. Conclusions

We have observed ENAs presumably from upstream of the bow shock that penetrate the martian system as we move into the eclipse. Simulations with ENA and UV models and a lack of correlation with photoelectrons emitted from the spacecraft suggest that the observed signal is not due to UV. There is also variability in the signal between different measurements suggesting the physical properties of the solar wind and/or the martian exosphere has changed. These measurements have brought about the idea of a new measurement technique that may be called ENA sounding by which solar wind and exospheric parameters can be determined from the spreading of ENAs into the eclipse of a planet.

Acknowledgments

The ASPERA-3 experiment on the European Space Agency (ESA) Mars Express mission is a joint effort between 15 laboratories in 10 countries, all sponsored by their national agencies. We thank all these agencies as well as the various departments/institutes hosting these efforts. This work was partially supported by the Swedish National Graduate School of Space Technology. Support for the Electron Spectrometer design, construction, operation and data analysis of the ASPERA-3 data was provided by NASA Contract NASW00003. We also acknowledge the Swedish National Space Board for their support of the main PI-institute and we are indebted to ESA for their courage in embarking on the Mars Express program, the first ESA mission to the red planet.

Appendix A. Count rate to flux conversion

The NPI sector count rate, C_{sector} , is converted to flux F via

$$F = \frac{C_{\text{sector}} - D_{\text{sector}}}{G_{\text{sector}} \cdot \epsilon_{\text{sector}}},$$

where D_{sector} is the sector dark count rate ($D_{22} = 11.5 \text{ s}^{-1}$), $G_{\text{sector}} = 2.7 \times 10^{-3} \text{ cm}^2 \text{ sr}$ is the geometrical factor of an NPI sector, and ϵ_{sector} is the NPI sector efficiency ($\epsilon_{22} = 10^{-3}$ is used, which is the calibrated efficiency for an energy of 1 keV).

The ELS integral flux, J determined for ELS sector 15 is obtained from the energy integral of the differential number flux intensity measurements between 5 and 10 eV,

$$J = \int_{5 \text{ eV}}^{10 \text{ eV}} j(E) dE,$$

where $j(E)$ is the energy dependent differential intensity. The energy dependent differential intensity for the ELS sector 15 is determined from

$$j(E) = \frac{C \cdot A \cdot K_{\text{sector}}}{G \cdot \Delta t \cdot E_c \cdot R \cdot T_{\text{MCP}} \cdot T_{\text{grid}} \cdot \epsilon_R \cdot \epsilon_A},$$

where C is the count rate (number of particles per accumulation for each energy step), A is the fractional difference between the theoretical anode azimuthal size and the manufactured anode azimuthal size ($A = 0.87$), K_{sector} is the fractional adjustment used to account for blockage of the field of view by the spacecraft ($K_{15} = 2.146711$), G is the physical geometric factor ($G = 5.88 \times 10^{-4} \text{ cm}^2 \text{ sr}$), Δt is the accumulation time width ($\Delta t = 28.125 \times 10^{-3} \text{ s}$), E_c is the energy of the step, R is the resolution ($R = \Delta E/E = 8.843 \times 10^{-2}$ for sector 15), T_{MCP} is the transparency of the MCP ($T_{\text{MCP}} = 0.58$), T_{grid} is the transparency of the protection grid ($T_{\text{grid}} = 0.81$), ϵ_R is the relative MCP efficiency (for sector 15, see below), ϵ_A is the absolute MCP efficiency ($\epsilon_A = 0.95$). Since sector 15 is used in this comparison, the relative MCP efficiency specifically for ELS sector 15 is

$$\begin{aligned} \epsilon_R = & 1714980 \times 10^{-6} + (-7089766 \times 10^{-9})V \\ & + 3259217 \times 10^{-11}V^2 + (-8410868 \times 10^{-14})V^3 \\ & + 1347052 \times 10^{-16}V^4 + (-1391524 \times 10^{-19})V^5 \\ & + 9397261 \times 10^{-23}V^6 + (-4114030 \times 10^{-26})V^7 \\ & + 1123482 \times 10^{-29}V^8 + (-1737531 \times 10^{-33})V^9 \\ & + 1161350 \times 10^{-37}V^{10}, \end{aligned}$$

where V is the voltage on the ELS deflection plate which corresponds to the energy of the step (E_c). For ELS sector 15, the deflection plate voltage and the energy of the step are related by

$$V = E_c S,$$

where S is the sensitivity (or k -factor) for sector 15 ($S = 7.188 \text{ eV V}^{-1}$).

References

- Acuña, M.H., and 19 colleagues, 1998. Magnetic field and plasma observations at Mars: Initial results of the Mars Global Surveyor mission. *Science* 279, 1676–1680.
- Acuña, M.H., and 12 colleagues, 1999. Global distribution of crustal magnetism discovered by the Mars Global Surveyor MAG/ER experiment. *Science* 284, 790–793.
- Barabash, S., Norberg, O., Lundin, R., Olsen, S., Lundin, K., C:son Brandt, P., Roelof, E.C., Chase, C., Mauk, B., 1998. Energetic neutral atom imager on the Swedish microsatellite Astrid. In: Pfaff, R.F., Borovsky, J.E., Young, D.T. (Eds.), *Measurement Techniques in Space Plasmas*. In: AGU Monographs, vol. 103. AGU, Washington, DC, pp. 257–262.
- Barabash, S., and 46 colleagues, 2004. ASPERA-3: Analyzer of Space Plasmas and Energetic Ions for Mars Express. ESA Special Publication SP-1240. ESA Publications Division, ESTEC, Noordwijk, The Netherlands, pp. 121–139.
- Brandt, P.C., Barabash, S., Roelof, E.C., Chase, C.J., 2001. ENA imaging at low altitudes from the Swedish microsatellite Astrid: Extraction of the equatorial ion distribution. *J. Geophys. Res.* 106 (A11), 25731–25744.
- Brandt, P.C., Demajistre, R., Roelof, E.C., Ohtani, S., Mitchell, D.G., Mende, S., 2002. IMAGE/HENA: Global energetic neutral atom imaging of the plasma sheet and ring current during substorms. *J. Geophys. Res.* 107 (A12), doi:10.1029/2002JA009307. 1454.
- Bush, B.C., Chakrabarti, S., 1995a. Analysis of Lyman α and He I 584-Å air-glow measurements using a spherical radiative transfer model. *J. Geophys. Res.* 100 (A10), 19609–19625.
- Bush, B.C., Chakrabarti, S., 1995b. A radiative transfer model using spherical geometry and partial frequency redistribution. *J. Geophys. Res.* 100 (A10), 19627–19642.
- Collier, M.R., and 18 colleagues, 2001. Observations of neutral atoms from the solar wind. *J. Geophys. Res.* 106, 24893–24906.
- Futaana, Y., and 45 colleagues, 2006a. First ENA observations at Mars: ENA emissions from the upper atmosphere. *Icarus* 182, 424–430.
- Futaana, Y., and 45 colleagues, 2006b. First ENA observations at Mars: Sub-solar ENA jet. *Icarus* 182, 413–423.
- Gunell, H., and 46 colleagues, 2005. First ENA observations at Mars: Charge exchange ENAs produced in the magnetosheath. *Icarus*. In press (this issue).
- Gunell, H., Holmström, M., Barabash, S., Kallio, E., Janhunen, P., Nagy, A.F., Ma, Y., 2006. Planetary ENA imaging: Effects of different interaction models for Mars. *Planet. Space Sci.* 54, 117–131.
- Holmström, M., Barabash, S., Kallio, E., 2002. Energetic neutral atoms at Mars. I. Imaging of solar wind protons. *J. Geophys. Res.* 107 (A10), doi:10.1029/2001JA000325.
- Kallio, E., 1996. An empirical model of the solar wind flow around Mars. *J. Geophys. Res.* 101, 11133–11147.
- Kallio, E., Luhmann, J.G., Barabash, S., 1997. Charge exchange near Mars: The solar wind absorption and energetic neutral atom production. *J. Geophys. Res.* 102, 22183–22197.
- Kallio, E. and 45 colleagues, 2006. Energetic neutral atoms (ENA) at Mars: Properties of the hydrogen atoms produced upstream of the martian bow shock and implications for ENA sounding technique around non-magnetized planets. *Icarus* 182, 448–463.
- Lundin, R., and 44 colleagues, 2004. Solar wind-induced atmospheric erosion at Mars: First results from ASPERA-3 on Mars Express. *Science* 305, 1933–1936.
- Lundin, R., and 44 colleagues, 2006. Ionospheric plasma acceleration at Mars: ASPERA-3 results. *Icarus* 182, 308–319.
- McKenna-Lawlor, S., Li, L., Barabash, S., Kudela, K., Balaz, J., Strharsky, I., Brinkfeldt, K., Gunell, H., Shen, C., Shi, J., Cao, J., Zong, Q., Fu, S., Roelof, E.C., Brandt, P.C., Dandouras, I., 2005. The NUADU experiment on tc-2 and the first energetic neutral atom (ENA) images recorded by this instrument. *Ann. Geophys.* 23 (8), 2825–2849.
- Mitchell, D.G., Jaskulek, S.E., Schlemm, C.E., Keath, E.P., Thompson, R.E., Tossman, B.E., Boldt, J.D., Hayes, J.R., Andrews, G.B., Paschalidis, N., Hamilton, D.C., Lundgren, R.A., Tums, E.O., Wilson, P., Voss, H.D., Prentice, D., Hsieh, K.C., Curtis, C.C., Powell, F.R., 2000. High Energy Neutral Atom (HENA) imager for the IMAGE mission. *Space Sci. Rev.* 91, 67–112.
- Mitchell, D.L., Lin, R.P., Mazelle, C., Rème, H., Cloutier, P.A., Connerney, J.E., Acuña, M.H., Ness, N.F., 2001. Probing Mars' crustal magnetic field and ionosphere with MGS electron reflectometer. *J. Geophys. Res.* 106 (A11), 23418–23427.
- Mitchell, D.G., Brandt, P.C., Roelof, E.C., Hamilton, D.C., Retterer, K.C., Mende, S., 2003. Global imaging of O⁺ from IMAGE/HENA. *Space Sci. Rev.* 109 (1–4), 63–75.
- Moore, T., and 23 colleagues, 2000. The low energy neutral atom imager for IMAGE. *Space Sci. Rev.* 91, 155–195.
- Taguchi, S., Collier, M.R., Moore, T.E., Fok, M.-C., Singer, H.J., 2004. Response of neutral atom emissions in the low-latitude and high-latitude magnetosheath direction to the magnetopause motion under extreme solar wind conditions. *J. Geophys. Res.* 109, doi:10.1029/2003JA010147. A04208.
- Tobiska, W.K., Woods, T., Eparvier, F., Viereck, R., Floyd, L., Bower, D., Rottman, G., White, O.R., 2000. The Solar2000 empirical solar irradiance model and forecast tool. *J. Atmos. Terr. Phys.* 62, 1233–1250.